Photometric Data from Non-Resolved Objects for Space Object Characterization and Improved Atmospheric Modeling

Richard Linares[*], Michael Shoemaker[†], Andrew Walker[‡], Piyush M. Mehta[§],
David M. Palmer[¶], David C. Thompson[‖], Josef Koller[**], John L. Crassidis[††]

1 Conference Paper

Accurate estimates for satellite drag coefficients are important in reducing the biases in densities derived from satellite drag measurements as well as explicitly reducing the errors in orbit prediction. This work develops an approach to estimate the drag coefficient for debris objects with known shape models. This paper focuses on rocket bodies in particular. The attitude and angular velocities are determined and orientation estimates are used to compute the drag coefficient using a flat plate model. A nonlinear least squares estimator is used to estimate the attitude and angular velocity of the space object. The technique is validated using both real data and simulated data scenarios. A number of representative rocket body models are used for the simulated and real data examples. Good performance is shown for both simulated and real data cases.

2 Introduction

The SSN network has the unique challenge of tracking more than 18,000 space objects (SOs) and providing critical collision avoidance warnings to military, NASA, and commercial systems. However, due to the large number of SOs and the limited number of sensors available to track them, it is impossible to maintain persistent surveillance. Observation gaps result in large propagation intervals between measurements and close approaches. Coupled with nonlinear SO dynamics, this results in difficulty in modeling the probability distribution functions (pdfs) of the SO. In particular, low-Earth orbiting (LEO) satellites are heavily influenced by atmospheric drag, which is very difficult to model accurately.

Los Alamos National Laboratory (LANL) has established a research effort, called IMPACT (Integrated Modeling of Perturbations in Atmospheres for Conjunction Tracking), to improve conjunction assessment via improved physics-based modeling. As part of this effort, calibration satellite observations are used to dynamically calibrate the physics-based model and to improve its forecasting capability. The observations are collected from a variety of sources, including LANL's own Raven-class optical telescope. This system collects both astrometric and photometric data on space objects. The photometric data will be used to estimate the space objects' attitude and shape.

A number of atmospheric models exist which can be classified as either empirical or physics-based models. The current Air Force standard is the High Accuracy Satellite Drag Model (HASDM), which is an empirical

[*]Graduate Student, Department of Mechanical and Aerospace Engineering, University at Buffalo, The State University of New York, Buffalo, NY 14260.

[†]Postdoctoral Research Associate, Space Science and Applications, ISR-1, Los Alamos National Laboratory, MS D466, Los Alamos, NM 87545.

[‡]Postdoctoral Research Associate, Space Science and Applications, ISR-1, Los Alamos National Laboratory, MS D466, Los Alamos, NM 87545.

[§]Graduate Research Assistant, Space Science and Applications, ISR-1, Los Alamos National Laboratory, MS D466, Los Alamos, NM 87545.

[¶]Senior Scientist, Space and Remote Sensing, ISR-2, Los Alamos National Laboratory, MS D466, Los Alamos, NM 87545.

[‖]Senior Scientist, Space and Remote Sensing, ISR-2, Los Alamos National Laboratory, MS D466, Los Alamos, NM 87545.

[**]Senior Scientist (IMPACT PI), Space Science and Applications, ISR-1, Los Alamos National Laboratory, MS D466, Los Alamos, NM 87545.

[††]Professor, Department of Mechanical and Aerospace Engineering, University at Buffalo, The State University of New York, Buffalo, NY 14260.

model based on observation of calibration satellites. These satellite observations are used to determine atmospheric model parameters based on their orbit determination solutions. Orbits passing within the atmosphere are perturbed by a number of factors including: density, drag coefficient, attitude, and shape of the space object. The satellites used for the HASDM model calibration process are chosen because of their relatively simple shapes, to minimize errors introduced due to shape mis-modeling. Under this requirement the number of calibration satellites that can be used for calibrating the atmospheric models is limited.

Simulations using computational methods, such as Direct Simulation Monte Carlo (DSMC), produce accurate estimates for the drag coefficient, but are too slow for real-time applications of orbit prediction for conjunction assessment. Therefore, modeling the drag coefficient is very important [1, 2]. In this work, we present a technique for extracting the drag coefficient from light curve measurements

Non-resolved photometric data have been studied as a mechanism for space object characterization. Photometry is the measurement of an object's flux or apparent brightness measured over a wavelength band. The temporal variation of photometric measurements is referred to as photometric signature. The photometric optical signature of an object contains information about shape, attitude, size and material composition [3–7]. This work focuses on the processing of the data collected with LANL's telescope in an effort to use photometric data to expand the number of space objects that can be used as calibration satellites.

Light curves (the SO temporal brightness) have also been used to estimate the shape of an object. Light curve techniques have been used to estimate the shape and state of asteroids [8, 9]. Reference [10] uses light curves and thermal emissions to recover the three-dimensional shape of an object assuming its orientation with respect to the observer is known. The benefits of using a light curve-based approach over the aforementioned techniques is that it is not limited to large objects in lower orbits and it can be applied to small and dim objects in higher orbits, such as geosynchronous. Here light curve data is considered for shape estimation, which is useful because it provides a mechanism to estimate both position and attitude, as well as their respective rates [3–7].

In the realm of spacecraft dynamics and orbit determination, the drag coefficient is defined in three distinct ways: (i) a fixed drag coefficient, (ii) a fitted drag coefficient, and (iii) a physical drag coefficient. Fitted drag coefficients are estimated as part of an orbit determination process and fixed drag coefficients simply use a constant value for the drag coefficient. Errors from the use of fixed drag coefficients arise because of the application of the value of 2.2 derived for compact satellites [11] to satellites with complex geometries or geometries with high aspect ratios such as a rocket bodies. For high aspect ratio objects, there can be a large amount of shear that drastically increases the drag coefficient. Meanwhile, multiple reflections for complex geometries can also lead to divergence from the commonly used value of 2.2. The drag coefficient also changes with altitude and solar conditions [12,13]. Fitted drag coefficients are specific to the atmospheric model used in the orbit determination process and therefore carry along the limitations of the atmospheric model and also frequently absorb other model errors. Physical drag coefficients are determined by the energy and momentum exchange of freestream atmospheric particles with the spacecraft surface [14]. Throughout this work, the term drag coefficients will refer to physical drag coefficients, unless stated otherwise.

The drag coefficient, characterized by the interaction between the atmosphere and the object, is an independent source of error whereas the errors in atmospheric mass density often stem from the use of fixed and/or fitted drag coefficients in its derivation from orbital drag measurements. Accurately deriving densities from drag measurements requires, in addition to accurate and high temporal resolution data (as in the case of an accelerometer), accurate modeling of the drag coefficient along the orbit. In addition, the use of fixed and/or fitted drag coefficients can by itself induce large orbit prediction errors.

Closed-form solutions for the drag coefficients of satellites with simple convex geometries like a sphere, cylinder, and cube in free molecular flow (FMF) were developed early in the Space Age [14, 15]; however, most satellites have complex shapes with concave geometries and require numerical modeling of the drag coefficient. The need for numerical modeling arises from multiple surface reflections and flow shadowing that changes the incident velocity distribution which is assumed to be Maxwellian for the analytic solutions. The drag coefficient in FMF is a function of the atmospheric translational temperature, T, surface temperature, T_w, spacecraft relative velocity, $\mathbf{v}_{\mathrm{rel}}$, chemical composition of the atmosphere, and gas-surface interaction (GSI) model.

The organization of this paper is as follows. First, the methodology is briefly discussed and following this, the shape models used in this work are discussed. Next, light curve and flux calculated models are shown.
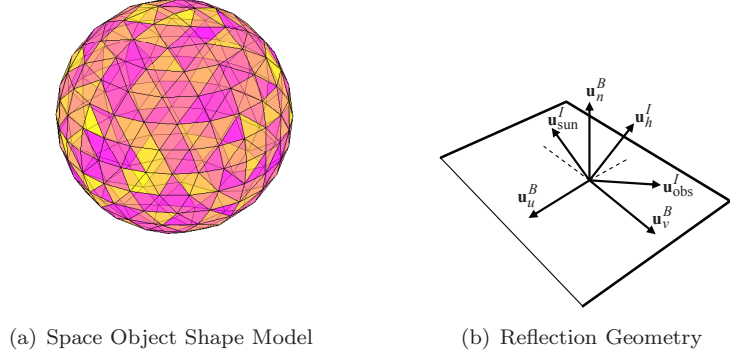
(a) Space Object Shape Model   (b) Reflection Geometry

Figure 1: Reflection Geometry and Space Object Shape Model

Then atmospheric drag model is shown and the analytical C_D expression for a flat plate model is shown and discussed. Following this, the nonlinear least squares approach used in this work is outlined. Finally, results are shown for simulated and real data examples, discussions, and conclusions are provided.

3   Shape Model Definition

The shape model considered in this work consists of a finite number of flat facets, where each facet has a set of basis vectors associated with it. These basis vectors are defined in Figure 1(b) and consist of three unit vectors $\mathbf{u}_n^B$, $\mathbf{u}_u^B$, and $\mathbf{u}_v^B$. The unit vector $\mathbf{u}_n^B$ points in the direction of the outward normal to the facet. For convex surfaces, this model becomes more accurate as the number of facets is increased. The vectors $\mathbf{u}_u^B$ and $\mathbf{u}_v^B$ are in the plane of the facet. The space objects (SOs) are assumed to be rigid bodies and therefore, the unit vectors $\mathbf{u}_n^B$, $\mathbf{u}_u^B$ and $\mathbf{u}_v^B$ do not change since they are expressed in the body frame.

The light curve and the solar radiation pressure (SRP) models discussed in the next sections require that these vectors be expressed in inertial coordinates and since the SO body is rotating, these vectors will change with respect to the inertial frame. The body vectors can be rotated to the inertial frame by the standard attitude mapping given by:

$$\mathbf{u}_k^B = A(\mathbf{q}_I^B)\mathbf{u}_k^I, \quad k = u,\, v,\, n \tag{1}$$

where $A(\mathbf{q}_I^B)$ is the attitude matrix mapping the inertial frame to the body frame using the quaternion parameterization. Furthermore, the unit vector $\mathbf{u}_{\text{sun}}^I$ points from the SO to the Sun direction and the unit vector $\mathbf{u}_{\text{obs}}^I$ points from the SO to the observer. The vector $\mathbf{u}_h^I$ is the normalized half vector between $\mathbf{u}_{\text{sun}}^I$ and $\mathbf{u}_{\text{obs}}^I$. This vector is also known as the Sun-SO-Observer bisector. Each facet has an area $\mathcal{A}(i)$ associated with it. Once the number of facets has been defined and their basis vectors are known, the areas $\mathcal{A}(i)$ define the size and shape of the SO. To determine the SRP forces and light curve characteristics, the surface properties must be defined for each facet.

The shape model used for this work use triangular facets defined by the location of their vertices $\mathbf{b}_i$. Then the area of the ith triangular facet formed by the convex hull of the control points is given by, $\mathcal{A}(i) = \|\mathbf{d}(i) \times \mathbf{l}(i)\|$, where $\mathbf{d}(i)$ and $\mathbf{l}(i)$ are the vectors defining two sides of the facets or $\mathbf{d}(i) = \mathbf{b}_i - \mathbf{b}_{i-1}$, $\mathbf{l}(i) = \mathbf{b}_i - \mathbf{b}_{i+1}$. The unit normal vector is given by

$$\mathbf{u}_n = \frac{\mathbf{d}(i) \times \mathbf{l}(i)}{\|\mathbf{d}(i) \times \mathbf{l}(i)\|} \tag{2}$$

For this work it is assumed that each facet has the same material parameters (specular coefficients, diffuse coefficients, and other reflection parameters discussed in the next section).
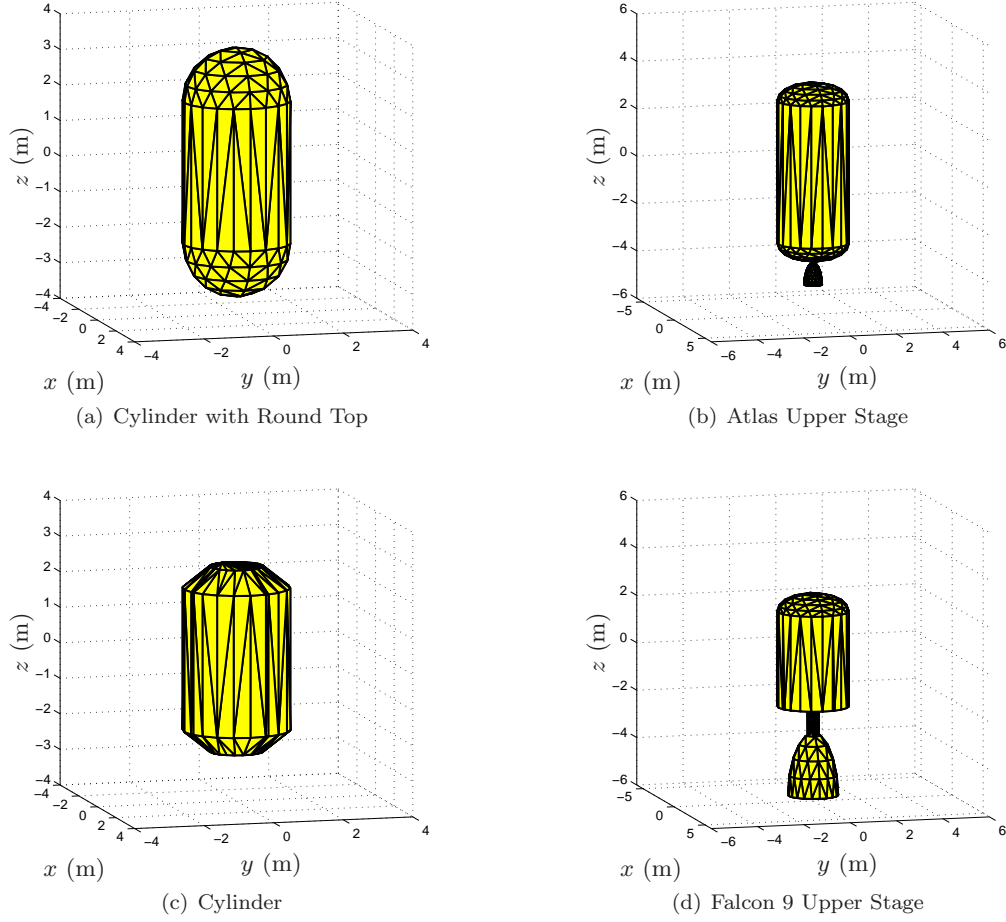
(a) Cylinder with Round Top

(b) Atlas Upper Stage

(c) Cylinder

(d) Falcon 9 Upper Stage

Figure 2: Representative Shape Models for Rocket Bodies

4 Ashikhmin-Shirley Model

In addition to the azimuth and elevation, the optical site also records the magnitude of the brightness of the SOs. The brightness of an object in space can be modeled using an anisotropic Phong light diffusion model or the Ashikhmin-Shirley model. [16] This model is based on the bidirectional reflectance distribution function (BRDF) which models light distribution scattered from the surface due to the incident light. The BRDF at any point on the surface is a function of two directions, the direction from which the light source originates and the direction from which the scattered light leaves the observed surface. The model in Ref. 16 decomposes the BRDF into a specular component and a diffuse component. The two terms sum to give the total BRDF:

$$\rho_{\text{total}}(i) = \rho_{\text{spec}}(i) + \rho_{\text{diff}}(i) \qquad (3)$$

The diffuse component represents light that is scattered equally in all directions (Lambertian) and the specular component represents light that is concentrated about some direction (mirror-like). Reference 16 develops a model for continuous arbitrary surfaces but simplifies for flat surfaces. This simplified model is employed in this work as shape models are considered to consist of a finite number of flat facets. Therefore the total observed brightness of an object becomes the sum of the contribution from each facet.

Under the flat facet assumption the specular term of the BRDF becomes [16]

$$\rho_{\text{spec}}(i) = \frac{\sqrt{(n_u(i) + 1)(n_v(i) + 1)}}{8\pi} \frac{\left(\mathbf{u}_n^I(i) \cdot \mathbf{u}_h^I\right)^z}{\mathbf{u}_n^I(i) \cdot \mathbf{u}_{\text{sun}}^I + \mathbf{u}_n^I(i) \cdot \mathbf{u}_{\text{obs}}^I - (\mathbf{u}_n^I(i) \cdot \mathbf{u}_{\text{sun}}^I)(\mathbf{u}_n^I(i) \cdot \mathbf{u}_{\text{obs}}^I)} F_{\text{reflect}}(i) \qquad (4)$$

4

where the exponent z is given by

$$z = \frac{n_u(i)(\mathbf{u}_h^I \cdot \mathbf{u}_u^I(i))^2 + n_v(i)(\mathbf{u}_h^I \cdot \mathbf{u}_v^I(i))^2}{(1 - (\mathbf{u}_h^I \cdot \mathbf{u}_n^I(i))^2)} \tag{5}$$

where the Fresnel reflectance is given by

$$F_{\text{reflect}}(i) = R_{\text{spec}}(i) + (1 - R_{\text{spec}}(i)) \left(1 - \mathbf{u}_{\text{sun}}^I \cdot \mathbf{u}_h^I\right)^5 \tag{6}$$

where R_{spec} is the specular reflectance coefficient. The parameters of the Phong model that dictate the directional (locally horizontal or vertical) distribution of the specular terms are n_u and n_v. The terms in Eq. (4) are functions of the reflection geometry which is described in Figure 1(b). The diffuse term of the BRDF is

$$\rho_{\text{diff}}(i) = \left(\frac{28 R_{\text{diff}}(i)}{23\pi}\right)(1 - R_{\text{spec}}(i)) \left[1 - \left(1 - \frac{\mathbf{u}_n^I(i) \cdot \mathbf{u}_{\text{sun}}^I}{2}\right)^5\right] \left[1 - \left(1 - \frac{\mathbf{u}_n^I(i) \cdot \mathbf{u}_{\text{obs}}^I}{2}\right)^5\right] \tag{7}$$

where $R_{\text{diff}}(i)$ is the diffuse coefficient for the ith side. The model discussed above assumes only single scattering and no self shadowing.

4.1   Flux Calculation

The apparent magnitude of an SO is the result of sunlight reflecting off of its surfaces along the line-of-sight to an observer. First, the fraction of visible sunlight that strikes an object (and is not absorbed) is computed by

$$F_{\text{sun}}(i) = C_{\text{sun,vis}} \left(\mathbf{u}_n^I(i) \cdot \mathbf{u}_{\text{sun}}^I\right) \tag{8}$$

where $C_{\text{sun,vis}} = 1062$ W/m^2 is the power per square meter impinging on a given object due to visible light striking the surface. If either the angle between the surface normal and the observer's direction or the angle between the surface normal and Sun direction is greater than $\pi/2$ then there is no light reflected toward the observer. If this is the case then the fraction of visible light is set to $F_{\text{sun}}(i) = 0$. Next, the fraction of sunlight that strikes an object that is reflected must be computed:

$$F_{\text{obs}}(i) = \frac{F_{\text{sun}}(i)\rho_{\text{total}}(i)\mathcal{A}(i)\left(\mathbf{u}_n^I(i) \cdot \mathbf{u}_{\text{obs}}^I\right)}{\|\mathbf{d}^I\|^2} \tag{9}$$

The reflected light of each facet is now used to compute the total photon flux, which is measured by an observer:

$$\tilde{F} = \left[\sum_{i=1}^{N} F_{\text{obs}}(i)\right] + v_{\text{CDD}} \tag{10}$$

where v_{CDD} is the measurement noise associated with flux measured by a Charge Coupled Device (CCD) sensor. The total photon flux is then used to compute the apparent brightness magnitude

$$m_{\text{app}} = -26.7 - 2.5\log_{10}\left|\frac{\tilde{F}}{C_{\text{sun,vis}}}\right| \tag{11}$$

where -26.7 is the apparent magnitude of the sun.

5   Atmospheric Drag

The drag acceleration on a satellite is defined by

$$\mathbf{a}_{\text{Drag}}^I = -\frac{1}{2}\frac{C_D \mathcal{A}}{m}\rho v_{rel}^2 \frac{\mathbf{v}_{rel}}{|\mathbf{v}_{rel}|} \tag{12}$$

where $\mathbf{a}_{\text{Drag}}^I$ is the drag force on the satellite, ρ is the mass density of the local atmosphere, $\mathbf{v}_{rel}$ is the relative velocity between the satellite and the co-rotating atmosphere, C_D is the satellite drag coefficient, A

is the projected area of the satellite normal to the velocity vector, and m is the satellite mass. In practice, $\mathcal{A}$ and m are well-known for attitude-stabilized artificial satellites while $\mathbf{v}_{rel}$ can be assumed to be accurately known in the absence of atmospheric winds.

The remaining two unknowns are ρ and C_D. For orbital propagation, ρ is generally taken from an empirical atmospheric model such as NRLMSISE-00. This leaves C_D as the only remaining unknown parameter. Early in the space age, it was common practice to simplify orbital propagation by using $C_D \sim 2.2$; however, theoretical work has shown that C_D can have large variations away from the constant value of 2.2. C_D is dependent on the atmospheric translational temperature, the speed of the satellite relative to the atmosphere, the satellite surface temperature, the atmospheric composition, the satellite surface composition, and the momentum and energy accommodation coefficients of the satellite surface.

Nearly all low Earth orbit satellites orbit at altitudes above $\sim$200 km where the atmosphere is free molecular. In free molecular flow, collisions between particles are so infrequent that they can be neglected. Under such conditions, closed-form solutions can be found for simple convex satellite geometries such as a sphere, flat plate, and cylinder. Closed-form solutions only exist for convex geometries because the concave geometries allow multiple reflections from the satellite surface and break a fundamental assumption of the solution that the incident velocity distribution function is Maxwellian.

The closed-form solution for the drag coefficient of a flat plate with a single side exposed to the flow is especially useful because any arbitrary geometry (convex or concave) can be decomposed into small flat plate elements. The total drag coefficient for an arbitrary geometry is then approximated as the sum of the drag coefficients of each of the flat plate elements. For convex geometries, the approximation converges to the true drag coefficient as the flat plate elements' size goes to zero. For concave geometries, the approximation does not account for multiple reflections from the satellite surface and is generally in error by a few percent.

Sentman [15] derived the closed-form solution for a flat plate with a single side exposed to the flow under the assumption of diffuse reflection. This solution assumes only single scattering and no self shadowing. The solution in terms of the angle of attack, θ, is given by

$$
\begin{aligned}
C_D = & \cos(\theta)\left(1 + \frac{1}{2s^2}\right)[1 + \mathrm{erf}(s\cos(\theta))] + \left(\frac{1}{\sqrt{\pi}s}\right)\exp\left\{-(s^2\cos^2(\theta))\right\} \\
& + \sqrt{\frac{T_{(k,r)}}{T_\infty}}\left[\frac{\sqrt{\pi}}{2s}\cos^2(\theta)\left(1 + \mathrm{erf}(s\cos(\theta))\right) + \left(\frac{\cos(\theta)}{2s^2}\right)\exp\left\{(-s^2\cos^2(\theta))\right\}\right]
\end{aligned}
\tag{13}
$$

The angle of attack is defined $\theta = \arccos(\mathbf{v}_{rel}^T \mathbf{u}_n)$. Here s is the speed ratio defined by

$$
s = \frac{|\mathbf{v}_{rel}|}{v_{mp}}
\tag{14}
$$

where v_{mp} is the most probable speed of a Maxwellian velocity distribution at the local translational temperature of the atmosphere, T_∞, and is defined by

$$
v_{mp} = \sqrt{\frac{2k_B T_\infty}{m_p}}
\tag{15}
$$

Here k_B is the Boltzmann constant and m_p is the atmospheric particle mass. The error function, $\mathrm{erf}(x)$, is defined as

$$
\mathrm{erf}(x) = \frac{2}{\sqrt{\pi}}\int_0^x e^{-t^2}\,dt
\tag{16}
$$

$T_{(k,r)}$ is the kinetic reflected temperature and is defined by

$$
T_{(k,r)} = T_{(k,i)}(1 - \alpha) + \alpha T_s
\tag{17}
$$

where α is the energy accommodation coefficient and $T_{(k,i)}$ is the kinetic incident temperature defined by

$$
T_{(k,i)} = \frac{m_p |\mathbf{v}_{rel}|^2}{3k_B}
\tag{18}
$$

When computing the drag coefficient for a mixture of gases, the total drag coefficient is the sum of the individual species drag coefficients weighted by the species mole fraction and particle mass and normalized by the average mass of the mixture, m_{avg}:

$$C_{(D,T)} = \frac{1}{m_{\mathrm{avg}}} \sum_{j=i}^{N} \chi_j m_j C_{D,j} \tag{19}$$

NRLMSISE-00 is used to compute the mole fractions χ_j for each specie. Here N is the total number of species and m_{avg} is computed from

$$m_{\mathrm{avg}} = \sum_{j=i}^{N} \chi_j m_j \tag{20}$$

Finally, the C_D for the faceted model is calculate by summing $C_{(D,T)}(i)$ for each facet, $i = 1, \ldots, N$

$$C_{(D,T)} = \frac{1}{\sum_{j=i}^{N} \mathcal{A} \cos(\theta) \phi} \sum_{j=i}^{N} C_{(D,T)}(i) \mathcal{A} \tag{21}$$

where $\phi = 1$ for $\phi < 90$ degs and $\phi = 0$ otherwise.

6 Nonlinear Least Squares

The estimation approach chosen for this work is the Nonlinear Least Squares (NLSQ) method. This method is a batch method and therefore it processes all the data at once. To apply the NLSQ method to attitude and angular velocity determination, one must linearize both the measurement and dynamic model. Also the attitude representation chosen for this work is the quaternion and therefore the attitude error must be approximated by a small angle error to avoid the quaternion unit constraint. The goal is to estimate a state $\mathbf{x}_k$ for times t_k from measurements $\mathbf{z}_k$ for $k = 1, \ldots, m$. Consider the following dynamic and measurement model, assuming m scalar measurements with uncorrelated measurement errors

$$\mathbf{x}_{k+1} = \mathbf{f}_k(\mathbf{x}_k) \tag{22a}$$
$$\mathbf{z}_k = \mathbf{g}_k(\mathbf{x}_k) + \mathbf{n}_k \tag{22b}$$

where $\mathbf{n}_i \sim \mathcal{N}(\mathbf{n}_i; 0, \Sigma_i^2)$ and $E\{\mathbf{n}_i \mathbf{n}_j\} = \delta_{ij} \Sigma_i^2$. Then Eq. (22a) and Eq. (22b) can be used to estimate the initial condition of the system, $\mathbf{x}_0$, by writing the measurements as $\mathbf{z}_k = \mathbf{g}_k(\phi_k(\mathbf{x}_0)) + \mathbf{n}_k$ where $\phi_k(\cdot)$ takes initial conditions and maps them to time k. The measurements can be written in vector form as

$$\mathbf{y} = \mathbf{h}(\mathbf{x}_0) + \mathbf{v} \tag{23}$$

where $\mathbf{y} = [\mathbf{z}_1, \ldots, \mathbf{z}_m]$, $\mathbf{v} \sim \mathcal{N}(\mathbf{v}; \mathbf{0}, R)$, $R = \mathrm{diag}(\Sigma_1^2, \ldots, \Sigma_m^2)$, and $\mathbf{h}(\cdot) = \mathbf{g}_k(\phi_k(\cdot))$. The system in Eq (22) can be solved using nonlinear least square by linearizing the system about the current estimate. Using a Taylor series expansion, the measurement function from Eq. (23) can be written as

$$\mathbf{h}(\mathbf{x}_o) = \mathbf{h}(\hat{\mathbf{x}}_o) + H(\hat{\mathbf{x}}_o)(\hat{\mathbf{x}}_o - \mathbf{x}_o) + \mathcal{O}(2) \tag{24}$$

where $H = \frac{\partial \mathbf{h}(\hat{\mathbf{x}}_o)}{\partial \mathbf{x}_o}\Big|_{\mathbf{x}_o = \hat{\mathbf{x}}_o} = \frac{\partial \mathbf{g}(\phi_k(\hat{\mathbf{x}}_o))}{\partial \phi_k} \frac{\partial \phi_k(\hat{\mathbf{x}}_o)}{\partial \mathbf{x}_o}\Big|_{\mathbf{x}_o = \hat{\mathbf{x}}_o}$. The derivatives of the measurement function $\mathbf{g}(\cdot)$ and the dynamic function $\phi_k(\cdot)$ must be calculated. The derivatives of $\mathbf{g}_k(\cdot)$ can be derived from the equations in section 4 and are shown in reference 17. The derivatives of $\phi_k(\cdot)$ involve the linearization of attitude kinematics and dynamic equations and these equations are shown later in the appendix. The NLSQ solution can be found by minimizing the following cost function

$$J(\mathbf{x}_o) = \frac{1}{2} [\mathbf{z} - \mathbf{h}(\mathbf{x}_i)]^T W [\mathbf{z} - \mathbf{h}(\mathbf{x}_i)] \tag{25}$$

where the weighting matrix is selected to be the inverse measurement covariance $W = R^{-1}$. The formal NLSQ iterative solution can be written as

$$\hat{\mathbf{x}}_o^{i+1} = \hat{\mathbf{x}}_o^i + [H_i^T W H_i]^{-1} H_i^T W [\mathbf{z} - \mathbf{h}(\mathbf{x}_i)] \tag{26}$$

where $P_o = E\{(\hat{\mathbf{x}}_o - \mathbf{x}_o)(\hat{\mathbf{x}}_o - \mathbf{x}_o)^T\}$ and $P_o = \left(H_i^T W H_i\right)^{-1}$ The estimate of $\mathbf{x}_o$ is obtained using Eq.(26) iteratively until a termination condition is met. Two conditions are set in this work, max number of iterations, $i_{\max}$, and relative tolerance

$$\epsilon = \frac{\|\hat{\mathbf{x}}_o^{i+1} - \hat{\mathbf{x}}_o^{i}\|}{\|\hat{\mathbf{x}}_o^{i}\|} \tag{27}$$

For this work $\epsilon = 0.1$ and $i_{\max} = 200$. This solution allows for a covariance to be computed for each time step by using P_o and the linearized dynamic equations. Then this covariance can be used to represent uncertainty in C_D that is computed from the orientation estimates.

(a) Attitude (Deg)   (b) Velocity Error (Deg/Hr)
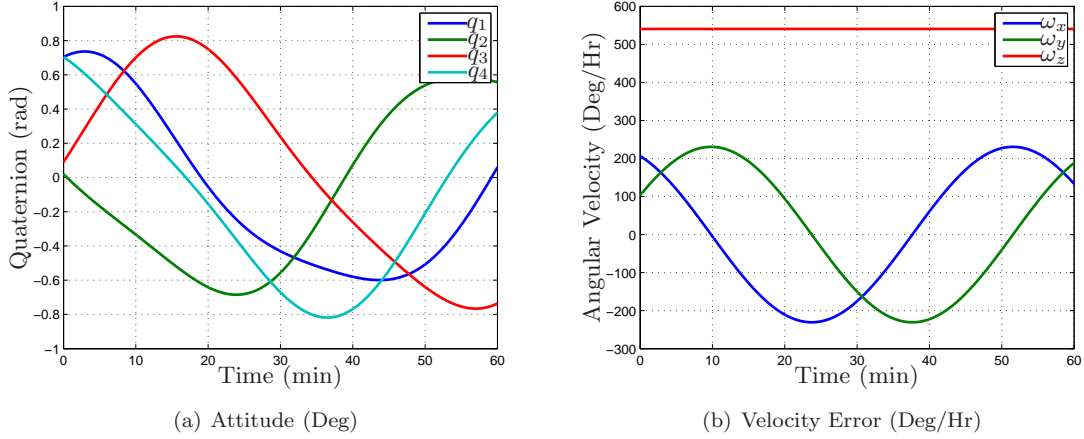
Figure 3: True Attitude and Angular Velocity Profile

7   SIMULATION RESULTS

This section discusses simulation results for the proposed method. Four examples are considered; each example uses different shape model. The shape models used are shown in Figure 2. The shape models used are; a cylinder with round top (Figure 2(a)), Atlas upper stage (Figure 2(b)), cylinder (Figure 2(c)), and a Falcon 9 upper stage (Figure 2(d)) model. Each model uses the same initial attitude and positions states and simulation conditions are given by

- Geographic position of the ground site is 0° North, 172° West with 0 km altitude

- The orbital elements are given by $a = 25864.16932$ km, $e = 0.743$, $i = 30.0083$ deg, $\omega = \Omega = 0.0$ deg and $M_0 = 91.065$ deg

- The initial time of the simulation is May 8, 2007 at 5:27.55 UTC

- Initial quaternion: $\mathbf{q}_I^B = [1/\sqrt{2} \; 0 \; 0 \; 1/\sqrt{2}]^T$

- A constant rotation rate, defined as the body rate with respect to the inertial frame (represented in body coordinates) is used given by $\boldsymbol{\omega}_{B/I}^B = [0 \; 0.00262 \; 0]^T$ rad/s

For all simulation scenarios, measurements of apparent magnitude are produced using zero-mean white-noise error processes with a standard deviation of 0.05 for magnitude. The initial errors for the states are 50 deg for all three attitudes, $1,000$ deg/hr for the rotational rate. The time interval between the measurements is set to 1 seconds and data are simulated for 1 hour. The simulation true quaternion and angular velocity are shown in Figure 3 and all simulation case have the same true orientational trajectories.

Figure 4 shows the simulated magnitude measurements for the models considered for this workusing Eq. (11). From this figure we can see that the simulate magnitude differ greatly for each rocket body model. The estimates found by the NLSQ approach for each case are shown in Figures 5, 6, 8, and 7. The simple cylinder model has the smallest variation since it has the smallest number of shape features and smoothest

(a) Cylinder with Round Top

(b) Atlas Upper Stage

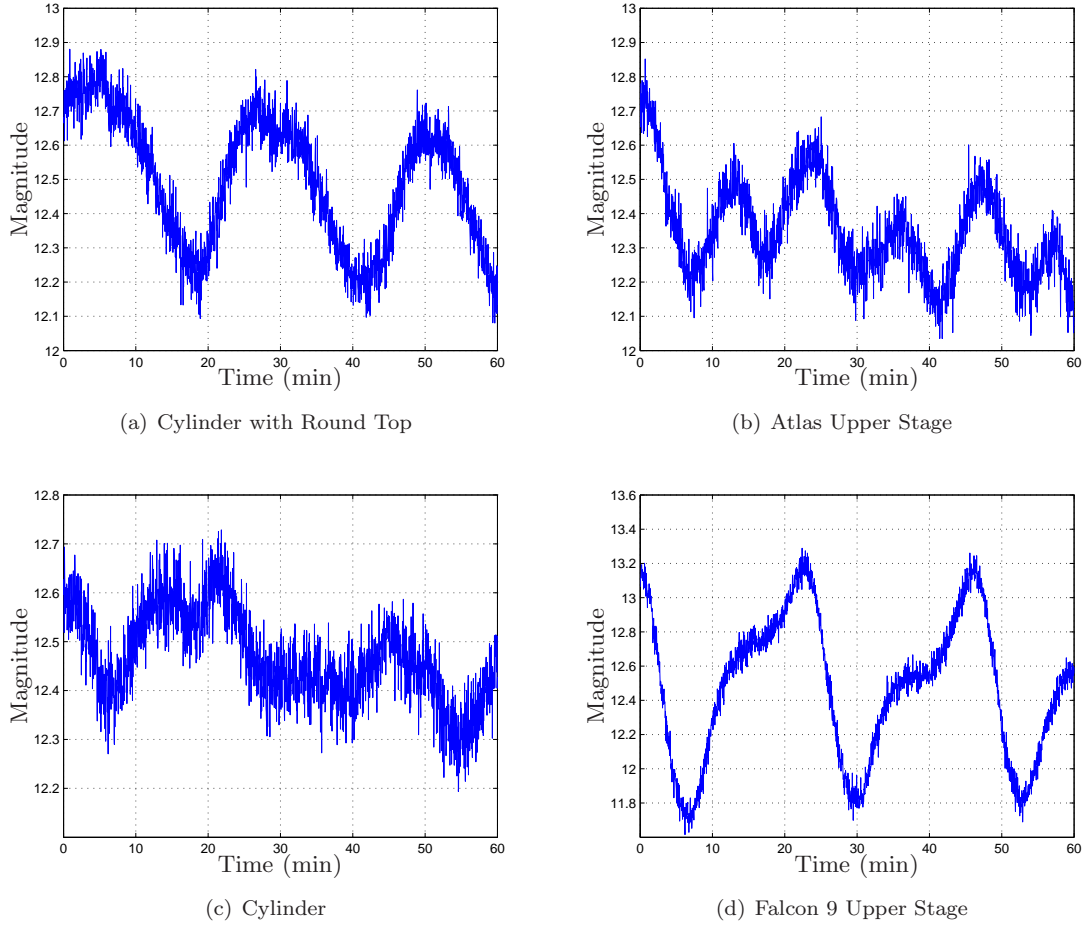(c) Cylinder

(d) Falcon 9 Upper Stage

Figure 4: Apparent Magnitude for Different Rocket Body Models

shape. The Falcon 9 upper stage has the greatest variation since it has a very large nozzle which provides a distinct feature in the light curve. The light curves of cylinder with round top model and atlas upper stage of similar magnitudes but the atlas upper stage has additional variation due to the small nozzle in its shape model. We can see from the simulation results that all the models shown good performance in terms of the measurement residual and by how well the predicted observations match the actual observation. However, since the light curves for the models are different they do not show the same observability in terms of the attitude and angular velocity estimated. In all cases except the a cylinder with round top the NLSQ approach converged to local solutions that do not make the true rotational states very well but fit the observations. This is due to the fact that these shapes have symmetries and therefore have multiple solutions. These ambiguities will be studied more in future work but the method can still predict the observations very well. From Figure 8 we can see that Falcon 9 rocket body shows the best attitude error of about 0.2 Degs, 0.2 Degs, and 5 Degs, in roll, pitch, and yaw, respectively.

Finally, the estimates from the NLSQ approach are used to compute C_D using the equations from section 5. These C_Ds are shown in Figure 10 for each rocket body model. From this figure, one can see that variations due to both rotation of the rocket bodies and changes in $\mathbf{v}_{\mathrm{rel}}$ due to orbital motion. The C_D values can be used to compute a mean C_D and a variance about that mean. This could be used to quantify the uncertainty in C_D if one assume a constant C_D. To highlight these variations Figure 9(b) shows the C_D values for altitudes less than 1000km for all models considered. This figure highlights how the shape geometry effects C_D, since each model has the same rotational dynamics, the variations shown here are due to geometry differences. Models that are similar like the Cylinder with Round Top and Cylinder have more similar C_D values, whereas the Falcon 9 Upper Stage has the largest difference from all other models. These

values could be used for orbit propagation and orbit determination directly.

The NLSQ approach provides a covariance for the estimated attitude and this along with unscented transformation discussed in Ref. 18 can be used to compute the variance in C_D due to attitude uncertainty considering the model in Eq. (13). The variance in C_D due to attitude uncertainty is shown in Figure 9(a) for the Round Top rocket body model along with the mean C_D estimate. From this figure it can be seen that the C_D 3σ does change along the trajectory and has different sensitivity at different altitudes.

(a) Measured and Estimated Magnitude

(b) Residual
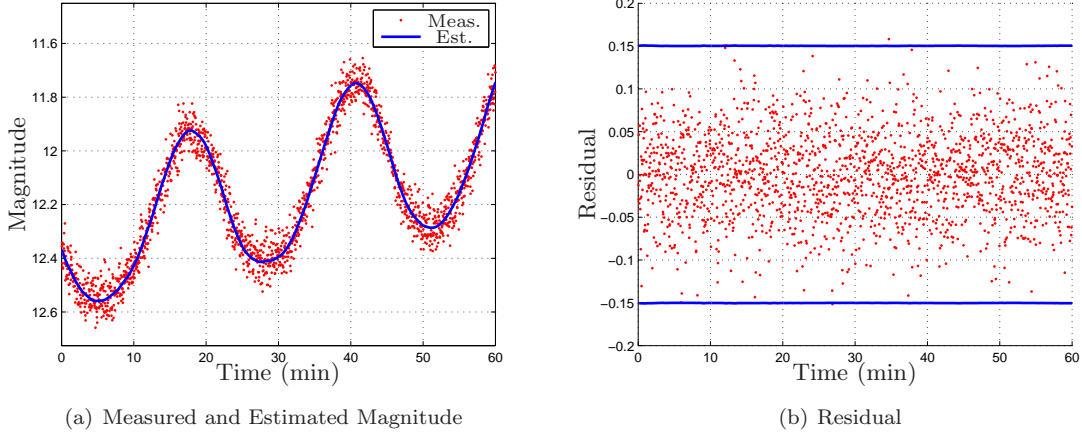
Figure 5: NLSQ Results for Cylinder with Round Top Rocket Body Model

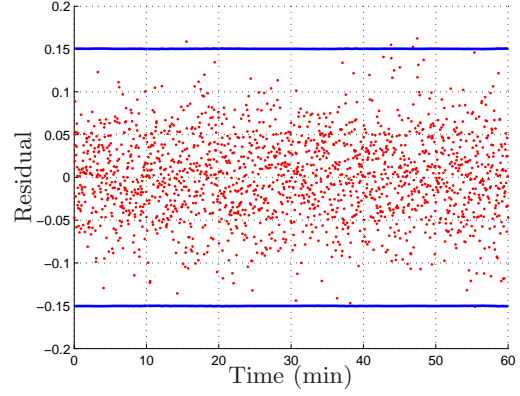(a) Measured and Estimated Magnitude

(b) Residual
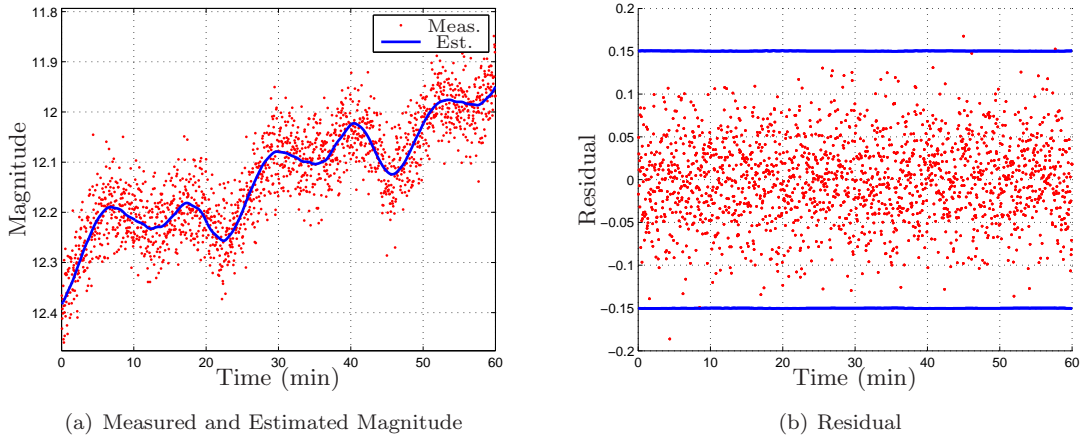
Figure 6: NLSQ Results for Cylinder Rocket Body Model

8 Actual Data Scenario

In this section, actual data from Los Alamos' satellite observation campaign was used. The data used in this example was gathered September 19 2012 03:29:30 UT. The object that was observed was an ARIANE 3 Rocket body with SSN number 15562. The observations were made with a small Raven-class telescope, located at LANL's high-altitude, dark site at Fenton Hill, NM. The observations were sampled every second for 5 mins. The simulation results for the real data example are shown in Figure 11. From Figure 11(c), we can see that the predicted magnitude fits the observations well and captures the main period of the light curve measurements. The estimated quaternion and angular velocity are shown in Figures 11(a) and 11(b). The orientation trajectory was recovered from actual data but more development is required until
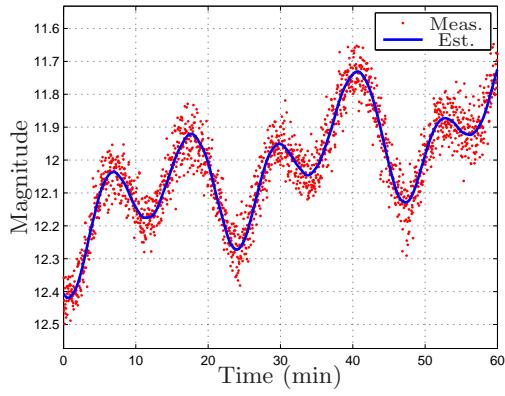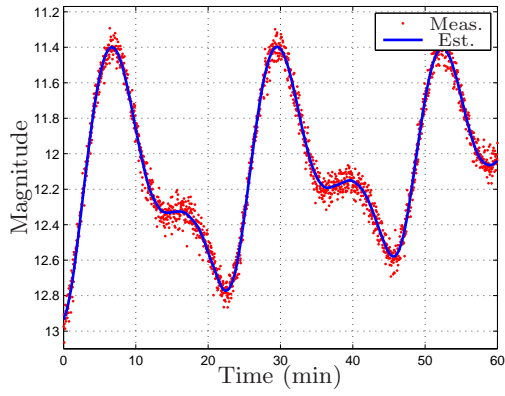
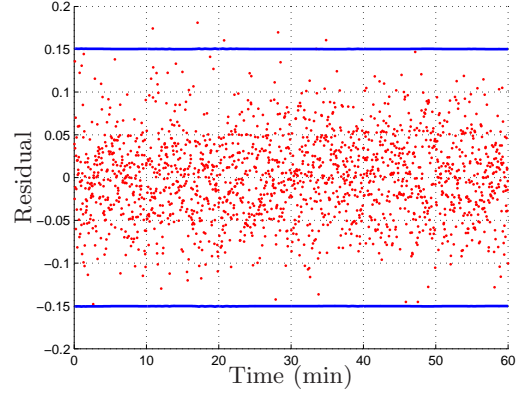(a) Measured and Estimated Magnitude

(b) Residual

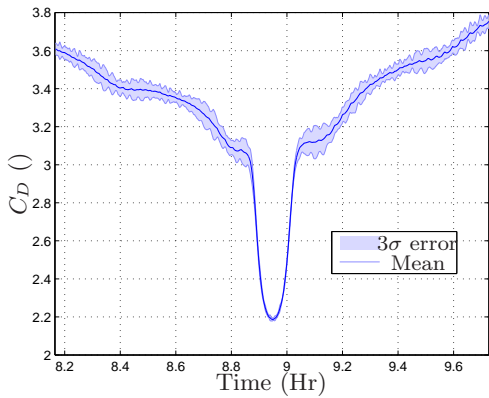Figure 7: NLSQ Results for Altas Rocket Body Model
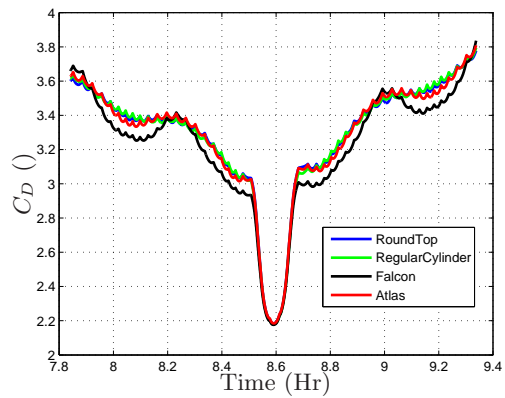

(a) Measured and Estimated Magnitude

(b) Residual

Figure 8: NLSQ Results for Falcon 9 Rocket Body Model

(a) The Uncertainty for the Round Top Rocket Body Model C_D

(b) Comparison of C_D Below 1000km

Figure 9: Comparison of C_D for Different Models

(a) Cylinder

(b) Cylinder with Round Top
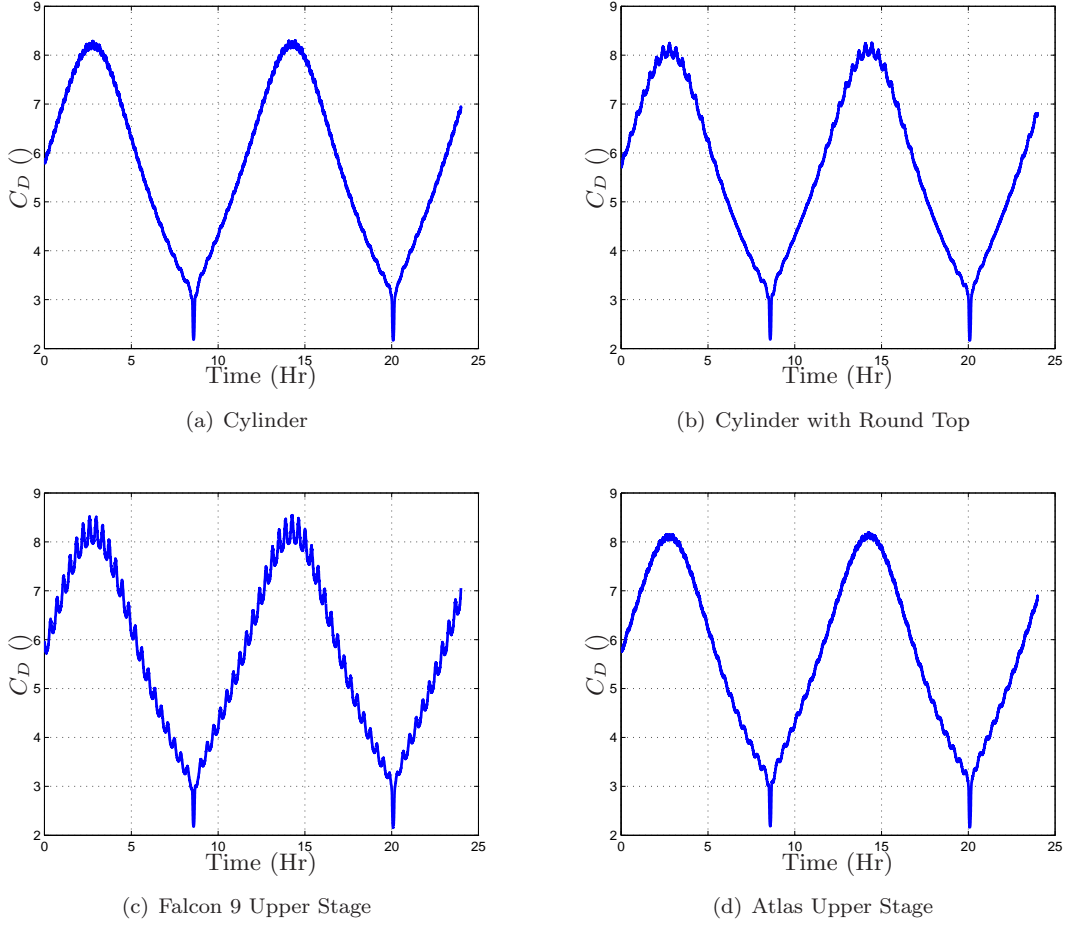
(c) Falcon 9 Upper Stage

(d) Atlas Upper Stage

Figure 10: Drag Coefficient For Different Rocket Body Models

this can provide improvement for orbit propagation, determination, or atmospheric density recovery. The measurement error must be understood better to allow for accurate uncertainty quantification.

9   Conclusions

In this paper, an Nonlinear Least Squares estimation scheme using light curve measurements was presented and used to estimate attitude and angular velocity of a space object (SO) with an assumed shape. This work focused on rocket bodies with perigee altitude lower than 300 km. The shape models consisted of triangular facets to allow for the modeling of complex rocket body shapes. Four different rocket body models were used: a simple cylinder, a simple cylinder with rounded top, a Falcon 9 upper stage, and an Atlas upper stage. The light curve model used was based on the Ashikhmin-Shirley BRDF and showed good performance for simulated and real data examples. The estimated orientation trajectories were used to estimate the drag coefficient of the SO over an orbit. This drag coefficient can then be used in orbit determination, orbit propagation, or to bound uncertainty of the drag coefficient over the orbit based on orientation variations. Future work will study the use of this approach along with the Tomography [19] method to recover density.

10   Appendix

In terms of the quaternion, the attitude matrix is given by

$$A(\mathbf{q}) = \Xi^T(\mathbf{q})\Psi(\mathbf{q}) \tag{28}$$

12

(a) Attitude (Deg)

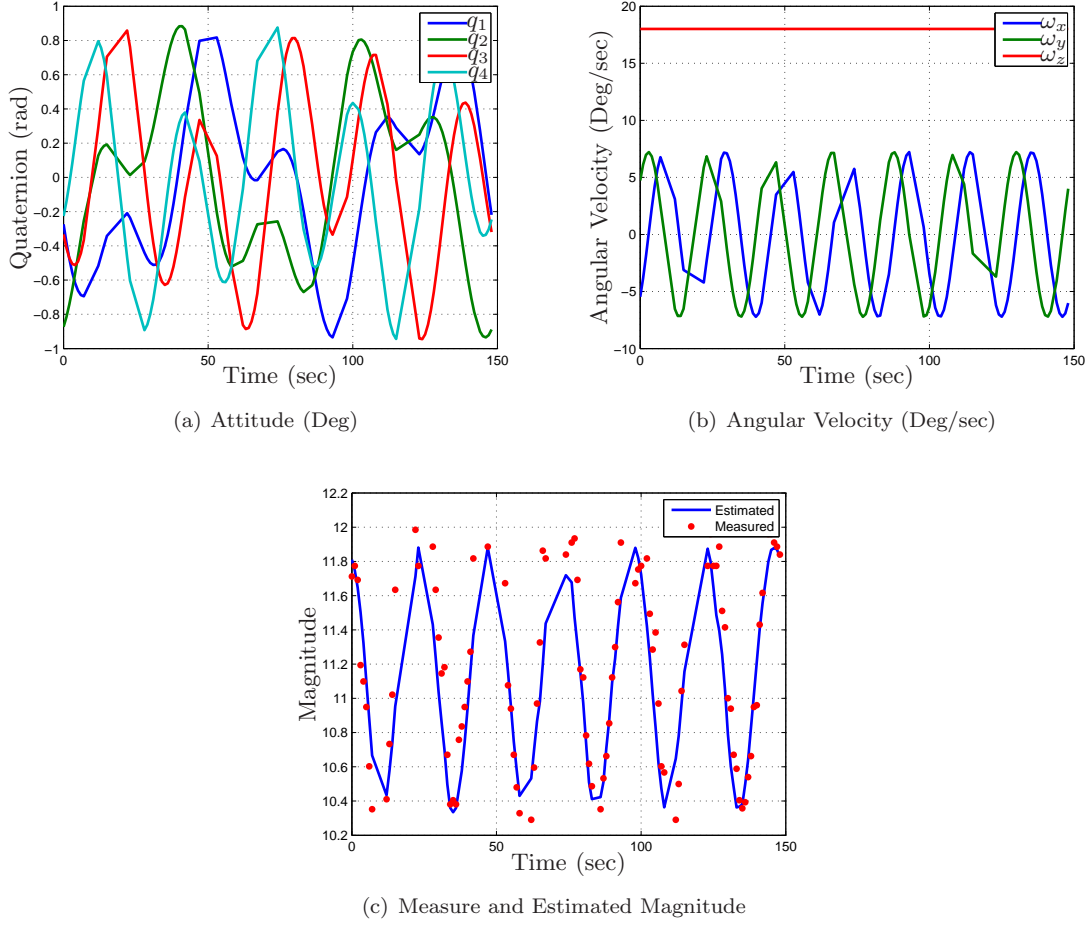(b) Angular Velocity (Deg/sec)

(c) Measure and Estimated Magnitude

Figure 11: Real Data Example

where

$$\Xi(\mathbf{q}) \equiv \begin{bmatrix} q_4 I_{3\times 3} + [\boldsymbol{\varrho}\times] \\ -\boldsymbol{\varrho}^T \end{bmatrix} \tag{29a}$$

$$\Psi(\mathbf{q}) \equiv \begin{bmatrix} q_4 I_{3\times 3} - [\boldsymbol{\varrho}\times] \\ -\boldsymbol{\varrho}^T \end{bmatrix} \tag{29b}$$

with

$$[\mathbf{a}\times] \equiv \begin{bmatrix} 0 & -a_3 & a_2 \\ a_3 & 0 & -a_1 \\ -a_2 & a_1 & 0 \end{bmatrix} \tag{30}$$

for any general 3×1 vector $\mathbf{a}$ defined such that $[\mathbf{a}\times]\mathbf{b} = \mathbf{a} \times \mathbf{b}$. This representation is constrained since the quaternion is of unit length and therefore $\mathbf{q}^T\mathbf{q} = 1$. The kinematics dynamics are given by a first-order differential equation:

$$\dot{\mathbf{q}} = \frac{1}{2}\Xi(\mathbf{q})\boldsymbol{\omega} \tag{31a}$$

$$\dot{\boldsymbol{\omega}}_{B/I}^B = J_{\text{SO}}^{-1}\left(-\left[\boldsymbol{\omega}_{B/I}^B\times\right] J_{\text{SO}}\boldsymbol{\omega}_{B/I}^B\right) \tag{31b}$$

13

11   Acknowledgement

References

[1] Mehta, P. M., McLaughlin, C. A., and Sutton, E. K., "Drag coefficient modeling for grace using Direct Simulation Monte Carlo," *Advances in Space Research*, 2013, pp. In Press.

[2] Mehta, P. M., Walker, A., Lawrence, E., Linares, R., Higdon, D., and Koller, J., "Modeling Satellite Drag Coefficients with Response Surfaces," *AAS/AIAA Astrodynamics Specialist Conference*, Hilton Head, South Carolina, 2013.

[3] Jah, M. and Madler, R., "Satellite Characterization: Angles and Light Curve Data Fusion for Spacecraft State and Parameter Estimation," *Proceedings of the Advanced Maui Optical and Space Surveillance Technologies Conference*, Vol. 49, Wailea, Maui, HI, Sept. 2007, Paper E49.

[4] Linares, R., Jah, M. K., and Crassidis, J. L., "Inactive Space Object Shape Estimation via Astrometric And Photometric Data Fusion," .

[5] Linares, R., Jah, M. K., and Crassidis, J. L., "Space Object Area-To-Mass Ratio Estimation Using Multiple Model Approaches," *Advances in the Astronautical Sciences*, Vol. 144, 2012, pp. 55–72.

[6] Linares, R., Jah, M. K., Crassidis, J. L., Leve, F. A., and Kelecy, T., "Astrometric and Photometric Data Fusion for Inactive Space Object Feature Estimation," *Proceedings of 62nd International Astronautical Congress, International Astronautical Federation*, Vol. 3, 2011, pp. 2289–2305.

[7] Linares, R., Leve, F. A., Jan, M. K., and Crassidis, J. L., "Space Object Mass-Specific Inertia Matrix Estimation From Photometric Data," *Advances in the Astronautical Sciences*, Vol. 144, 2012, pp. 41–54.

[8] Kaasalainen, M. and Torppa, J., "Optimization Methods for Asteriod Lightcurve Inversion I: Shape Determination," *Icarus*, Vol. 153, No. 4, Jan. 2001, pp. 24–36.

[9] Kaasalainen, M. and Torppa, J., "Optimization Methods for Asteriod Lightcurve Inversion II: The Complete Inverse Problem," *Icarus*, Vol. 153, No. 4, Jan. 2001, pp. 37–51.

[10] Calef, B., Africano, J., Birge, B., Hall, D., and Kervin, P. W., "Photometric Signature Inversion," *Proceedings of the International Society for Optical Engineering*, Vol. 6307, San Diego, CA, Aug. 2006, Paper 11.

[11] Cook, G. E., "Satellite drag coefficients," *planss*, Vol. 13, Oct. 1965, pp. 929.

[12] Walker, A., Mehta, P. M., and Koller, J., "A Quasi Specular Drag Coefficient Model using the Cercignani Lampis Lord Gas Surface Interaction Model," *Journal of Spacecraft and Rockets in press*, 2013.

[13] Mehta, P. M., Walker, A., McLaughlin, C. A., and Koller, J., "Comparing Physical Drag Coefficients Computed with Direct Simulation Monte Carlo using different Gas-Surface Interaction Models," *Journal of Spacecraft and Rockets in press*, 2013.

[14] Schaaf, S. A. and Chambré, P. L., *Flow of rarefied gases*, Princeton University Press Princeton, 1961.

[15] Sentman, L., Missiles, L., and Company, S., *Free Molecule Flow Theory and Its Application to the Determination of Aerodynamic Forces*, LMSC-448514, Lockheed Missiles & Space Company, a division of Lockheed Aircraft Corporation, 1961.

[16] Ashikmin, M. and Shirley, P., "An Anisotropic Phong Light Reflection Model," Tech. Rep. UUCS-00-014, University of Utah, Salt Lake City, UT, 2000.

[17] Hinks, J. C., Linares, R., and Crassidis, J. L., "Attitude Observability from Light Curve Measurements," *AIAA Guidance, Navigation, and Control (GNC) Conference*, No. 10.2514/6.2013-5005, AIAA, Boston, MA, 2013.

[18] Julier, S. J., Uhlmann, J. K., and Durrant-Whyte, H. F., "A New Method for the Nonlinear Transformation of Means and Covariances in Filters and Estimators," *IEEE Transactions on Automatic Control*, Vol. AC-45, No. 3, March 2000, pp. 477–482.

[19] Shoemaker, M. A., Wohlberg, B., Linares, R., and Koller, J., "Application of Optical Tracking and Orbit Estimation to Satellite Orbit Tomography," *AAS/AIAA Astrodynamics Specialist Conference*, 2013.